

# Clifford Deformed Compass Codes

Julie A. Campos<sup>1,2,\*</sup> and Kenneth R. Brown<sup>1,2,3,4,†</sup>

<sup>1</sup>*Duke Quantum Center, Duke University, Durham, NC 27701, USA*

<sup>2</sup>*Department of Physics, Duke University, Durham, NC 27708, USA*

<sup>3</sup>*Department of Electrical and Computer Engineering, Duke University, Durham, NC 27708, USA*

<sup>4</sup>*Department of Chemistry, Duke University, Durham, NC 27708, USA*

(Dated: December 6, 2024)

We can design efficient quantum error-correcting (QEC) codes by tailoring them to our choice of quantum architecture. Useful tools for constructing such codes include Clifford deformations and appropriate gauge fixings of compass codes. In this work, we find Clifford deformations that can be applied to elongated compass codes resulting in QEC codes with improved performance under noise models with errors biased towards dephasing commonly seen in quantum computing architectures. These Clifford deformations enhance decoder performance by introducing symmetries, while the stabilizers of compass codes can be selected to obtain more information on high-rate errors. As a result, the codes exhibit thresholds that increase with bias and display lower logical error rates. One of the Clifford deformations we explore yields QEC codes with better thresholds and logical error rates than those of the XZZX surface code at moderate biases.

## I. INTRODUCTION

The advancement of quantum computers is limited by noise leading to errors in computation. One way to handle these errors is by using quantum error-correcting (QEC) [1] codes to encode logical qubits in several physical qubits. By doing this, the logical error rate can be suppressed exponentially, enabling us to achieve fault-tolerant computation when the physical error rate is less than a threshold value [2, 3].

While depolarizing noise is the most common choice of error model when evaluating the performance of a QEC code [4–7], it is not the most representative of real noise. The depolarizing noise model assumes that any Pauli error can occur with the same probability, but it is often the case that quantum systems exhibit a more structured noise model and in some cases qubits are engineered to experience biased noise. For example, superconducting cat qubits can be designed to have dominant Pauli- $X$  or Pauli- $Z$  errors [8–11]. Additionally, there are methods to engineer bias toward erasure errors in superconducting [12–14], neutral atom [15, 16] and trapped ion qubits [17]. In this work, we are primarily motivated by noise models with dominant dephasing errors which have been observed in trapped ion [18, 19], spin [20] and superconducting qubits [21, 22].

A benefit of having biased errors in quantum computing architectures is that we can design QEC codes that extract more information on dominant errors. The resulting codes can achieve high thresholds under biased noise models [23–30]. Two examples of such codes are the XZZX surface code [27] and elongated compass codes [26, 31] which are effective at detecting and correcting

errors biased toward dephasing.

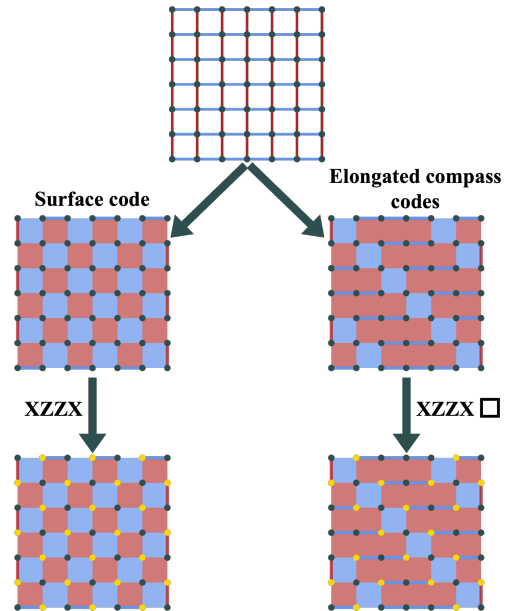


Figure 1: Starting with weight-2 gauge operators ( $Z$  in red,  $X$  in blue, qubits are gray dots) corresponding to the interaction terms of the quantum compass model Hamiltonian, we construct stabilizer codes through gauge fixing. The surface code and elongated compass codes (here with  $\ell = 4$ ) are examples of such codes. By applying a Clifford deformation on the surface code we obtain the XZZX surface code which has improved performance under biased noise models. Yellow dots indicate qubits which undergo a Hadamard transformation. The elongated compass codes perform better than the surface code under biased noise models, but can be improved further by applying the XZZX Clifford deformation introduced in this work.

\* julie.campos@duke.edu

† ken.brown@duke.edu

Elongated compass codes are a class of 2D compass codes [26] which result from a choice of fixed gauges [32, 33]. The stabilizers of elongated compass codes are determined by the elongation parameter, which dictates the amount of weight-2  $X$  stabilizers. As the number of these weight-2  $X$  stabilizers increases, the code can detect and correct more  $Z$  errors. Compass codes have also been studied under noise models with coherent errors [34].

The XZZX surface code is equivalent to the surface code [35–37] up to the application of a Hadamard transformation on every other qubit. This simple modification to the surface code stabilizers introduces a symmetry that can provide extra information about the location of errors to the decoder (Figure 2). This characteristic of the XZZX surface code leads it to have a threshold of 50% under a noise model with infinite bias towards any Pauli error.

The XZZX surface code is an example of a Clifford deformation of the surface code [29, 30]. The Clifford deformation of a stabilizer code refers to the modification of the stabilizers through the application of a set of single-qubit Clifford operators. There have been extensive studies on the application of this procedure to surface codes [23, 27, 29, 30] and similar procedures have been developed for color codes [38, 39]. Clifford deformed codes have been implemented in experiments. A Pauli deformed Shor code was shown to improve quantum memories in a logical qubit in trapped ions [40]. The XZZX surface code has been implemented experimentally in a superconducting qubit platform [41].

In this work, we explore sets of Clifford deformations that add structure to the stabilizers of the elongated compass codes leading to improved thresholds and logical error rates under biased noise models. To preserve the advantage of the elongated compass codes, we consider two sets of Clifford deformations we call the XZZX□ and the ZXXXZ□ deformations (Figure 3). These deformations are chosen to preserve the weight-2  $X$  stabilizers of the elongated compass codes while introducing a symmetry that restricts the spread of defects.

The paper is structured as follows. The noise model is defined in Section II A. Compass codes and elongated compass codes are described in more detail in Section II B. We introduce the Clifford deformations we apply to the elongated compass codes in Section II C. In Section II D, we give a brief description of the minimum-weight perfect matching (MWPM) algorithm as our decoder. In this section, we also discuss how Clifford deformations affect the decoder graphs. Finally, thresholds and logical error rate comparisons are reported and discussed in Section III. Concluding remarks are in Section IV.

## II. CODES AND NOISE MODEL

### A. Noise Model

We consider a single-qubit Pauli noise channel where all qubits can experience a Pauli error with probability  $p = p_x + p_y + p_z$ . Here,  $p_x, p_y$  and  $p_z$  correspond to the probabilities of  $X, Y$  and  $Z$  errors respectively. These errors occur independently and uniformly across the lattice. The noise channel is expressed in the following way:

$$\mathcal{E}[\rho] = (1 - p)\rho + p_x X\rho X + p_y Y\rho Y + p_z Z\rho Z \quad (1)$$

We assume that the errors are biased towards dephasing which, in Pauli representation of the noise channel, is a bias towards Pauli- $Z$  errors. This bias is quantified by  $\eta = \frac{p_z}{p_x + p_y}$ . For simplicity, we assume  $p_x = p_y$ . We obtain the depolarizing channel when  $\eta = 0.5$ . In several quantum architectures,  $\eta$  can reach values as high as  $10^2$  [8, 9]. Motivated by this, we evaluate our codes under biased noise models with  $0.5 \leq \eta \leq 100$ .

### B. Elongated Compass Codes

Compass codes are subsystem stabilizer codes [42, 43] whose stabilizer group  $\mathcal{S}$  [44] results from a choice of gauge fixes [32, 33]. The complete gauge group from which we start is generated by the interaction terms of the 2D quantum compass model Hamiltonian [45–47] on a square lattice:

$$\hat{H} = -J_X \sum_{i=0}^{L-2} \sum_{j=0}^{L-1} \hat{X}_{i,j} \hat{X}_{i+1,j} - J_Z \sum_{i=0}^{L-1} \sum_{j=0}^{L-2} \hat{Z}_{i,j} \hat{Z}_{i,j+1} \quad (2)$$

Let  $(i, j)$  denote the coordinate of a qubit on a square lattice of size  $L \times L$ , then the generators of the gauge group are of the form  $\hat{X}_{i,j} \hat{X}_{i+1,j}$  where  $(i, j) \in [0, L-2] \times [0, L-1]$  and  $\hat{Z}_{i,j} \hat{Z}_{i,j+1}$  where  $(i, j) \in [0, L-1] \times [0, L-2]$  (Figure 1).

One can go between distinct compass codes by fixing a different set of gauges [32, 33]. Some well-known compass codes include the Bacon-Shor code [48, 49] and the surface code [35, 36]. Here, we focus on the elongated compass codes which are appropriate for correcting dominant  $Z$  errors [26]. Elongated compass codes are classified according to an elongation parameter  $\ell$ . To illustrate the process of gauge fixing to obtain elongated compass codes, we label the coordinates of the plaquettes on the lattice  $(i, j)$  where the origin is at the top left. Then, we fix the product of the  $X$  gauges that are supported by qubits on the plaquettes with  $i - j \equiv 0 \pmod{\ell}$ , creating weight-4  $X$  stabilizers. In each row, we fix the product of  $Z$  gauges between the  $X$  stabilizers we fixed. The resulting  $Z$  stabilizers are rectangles of length  $\ell - 1$  and

weight  $2\ell$ . Finally, we fix all of the remaining weight-2  $X$  gauges surrounding the  $Z$  stabilizer rectangles ensuring commutativity of all stabilizers. See Figure 1 for a depiction of an elongated compass code with  $\ell = 4$ . An elongated compass code with  $\ell = 2$  is the rotated surface code (Figure 1). Note that elongated compass codes are Calderbank-Shor-Steane (CSS) codes since their stabilizers are either a product of only Pauli- $X$  or only Pauli- $Z$  [1, 50].

As the elongation parameter grows, the  $X$  and  $Z$  stabilizers become more asymmetric (Figure 3). The increasing weight of the  $Z$  stabilizers makes them less informative about  $X$  errors, but by gaining more weight-2  $X$  stabilizers, we obtain more information on  $Z$  errors. This leads to a trade-off in the  $X$  and  $Z$  decoding performance as the bias increases. A consequence of this trade-off is that there is an optimal bias at which elongated compass codes achieve a maximum threshold [26]. The optimal bias balances the performance of the  $X$  and  $Z$  decoders for depolarizing noise. The optimal biases ( $\eta_\ell^*$ ) found in [26] for elongated compass code with  $\ell = 2, 3, 4, 5, 6$  are  $\eta_2^* = 0.5$ ,  $\eta_3^* = 1.67$ ,  $\eta_4^* = 3.0$ ,  $\eta_5^* = 4.26$ , and  $\eta_6^* = 5.89$ . The maximum threshold reached at the optimal bias increases with elongation parameter making higher elongations desirable for higher biases.

### C. Clifford Deformations

Clifford deformations are modifications of stabilizer codes that can lead to significant improvements in codes' thresholds under biased noise models [23, 27, 29, 30, 39]. The Clifford deformation of a stabilizer code is the application of an arbitrary set of single-qubit unitary transformations from the Clifford group on the codespace. Clifford transformations map Pauli operators to other Pauli operators and thus preserve the stabilizer structure of the code. Additionally, a Clifford deformation preserves the weight and support qubits of the stabilizers. However, one possible consequence of a Clifford deformation is that the resulting code may be non-CSS since the operators making up the stabilizers are modified. For example, the XZZX surface code is not a CSS code.

The XZZX surface code [27] results from a Clifford deformation of the surface code where a Hadamard transformation is applied on every other qubit of the lattice (Figure 2). All plaquette stabilizers acquire the form XZZX, giving the code its name. This change introduces a symmetry which restricts the propagation of defects to one dimension. Regardless of their location,  $X$  or  $Z$  errors will produce defects aligned in a particular direction. Furthermore, these directions are perpendicular to each other. We can see this from Figures 2c and 2d which depict the directions in which  $Z$  and  $X$  defects spread respectively. Since defects are restricted to

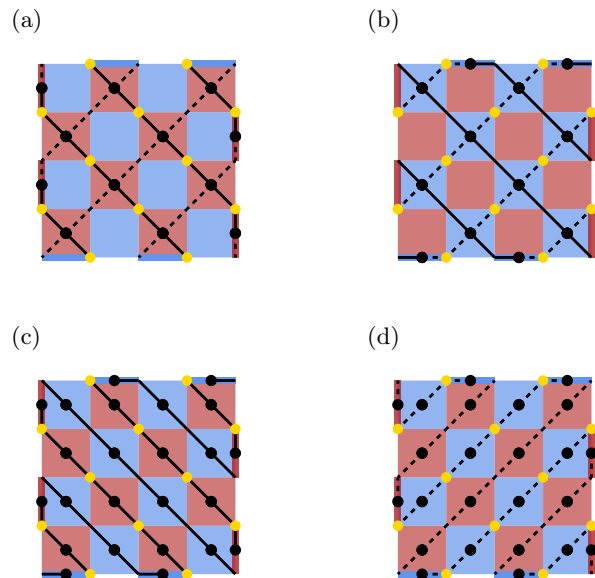


Figure 2: **XZZX surface code** Decoder graphs for **a)**  $Z$  stabilizers (in red) and **b)**  $X$  stabilizers (in blue) of the surface code (elongated compass code with  $\ell = 2$ ). Qubits lie on the vertices of the lattice and those with yellow dots undergo a Hadamard transformation according to the XZZX deformation. Black dots are vertices of the decoder graph and correspond to stabilizers. Edges of the decoder graphs travel across the qubit locations. Solid edges have a low weight (high error probability) and dashed edges have a high weight (low error probability). These graphs are more relevant at low biases since the distinction between the solid and dashed lines is less significant. The combination of the low(high)-weight edges from **a** and **b** results in the matching graph shown in **c**(**d**). As the bias increases, the decoding graph **c** dominates the decoding procedure.

one dimension, a pair of defects aligned in one of these directions will be the endpoints of a string of errors of the same type. This allows us to decode Pauli- $X$  and Pauli- $Z$  errors as disjoint sets of repetition codes under noise models with infinite bias.

The XZZX surface code outperforms the CSS surface code under all biased Pauli noise models and even surpasses the hashing bound for some biases [27]. We can understand the improvement over the CSS surface code by noting that the surface code stabilizers gather more information about  $Y$  errors than  $X$  and  $Z$  errors. In general, this is a consequence of the fact that all surface code stabilizers are sensitive to  $Y$  errors giving us more syndrome bits. As a result, the surface code does well under biased noise models only if the bias is towards  $Y$  errors [23, 24]. In contrast, the additional symmetries

of the XZZX surface code provide additional information on  $X$  and  $Z$  errors to the decoder, making the code efficient in the case of any Pauli bias.

We could apply the XZZX deformation to elongated compass codes in the same way it was applied to the surface code to get the XZZX surface code. That is, we could apply a Hadamard transformation on every other qubit. However, this is not ideal for elongated compass codes because it will change the weight-2  $X$  stabilizers, removing the advantage of the elongated compass codes. Instead, we consider a similar Clifford deformation that applies a Hadamard transformation to the top right and bottom left qubits supporting weight-4  $X$  stabilizers (Figures 1 and 3). After doing this, the weight-4  $X$  stabilizers become of the form XZZX. We refer to the resulting codes as the XZZX $\square$ -deformed compass codes.

Another deformation we consider is the ZXXZ $\square$  deformation. This deformation applies Hadamard transformations on the top left and bottom right qubits of the weight-4  $X$  stabilizers (Figure 3). The ZXXZ $\square$  deformation only changes the weight-2  $X$  stabilizers in the top and bottom rows of the code while the XZZX $\square$  deformation affects all rows. In the case of  $\ell = 2$ , the ZXXZ $\square$  deformation is equivalent to the XZZX and XZZX $\square$  deformations since it only switches the directions in which the low and high-weight edges are aligned (Figure 2).

#### D. Decoder

We use a minimum-weight perfect matching (MWPM) decoder and implement the algorithm using pyMatching [51, 52]. The input of the MWPM algorithm is a weighted graph  $\mathcal{G} = (\mathcal{V}, \mathcal{E}, \mathcal{W})$  where  $\mathcal{V} = \{v_i\}$ ,  $\mathcal{E} = \{e_{ij}\} = \{(v_i, v_j)\}$  and  $\mathcal{W} = \{w_{ij}\}$  are sets of vertices, edges and weights respectively. The vertices of the graph correspond to stabilizers, the edges correspond to qubits, and the weights of each edge are a logarithmic function of the probability of error of the qubit it corresponds to ( $w = \log\left(\frac{1-p}{p}\right)$ ). A matching  $M$  is a subset of disjoint edges in  $E$ . A perfect matching is a matching such that  $\forall v \in \mathcal{V}, \exists e \in M$  s.t.  $v \in e$ . Thus, the MWPM of a graph is a perfect matching that minimizes the sum of the weights in the matching. The output is a set of edges that correspond to the most probable set of errors.

In the case of a CSS code,  $X$  and  $Z$  syndromes can be decoded independently by running the MPWM algorithm on  $X$  and  $Z$  decoder graphs. This simplifies decoding since we are dividing the decoding problem into two. The XZZX $\square$  and ZXXZ $\square$ -deformed codes we consider are not CSS codes, which means that we can't decode them in this way directly. However, we can get around this by considering that our decoding problem is equivalent to that of decoding a CSS code under an inhomogeneous noise model.

We set the stage by letting  $\mathcal{C}_\ell$  denote a CSS compass

code with elongation parameter  $\ell$  and  $\mathcal{C}'_\ell$  be a Clifford deformation of  $\mathcal{C}_\ell$ . The Clifford deformation we apply to  $\mathcal{C}_\ell$  to obtain  $\mathcal{C}'_\ell$  is  $\{U_q\}_{q=0}^N$  where  $U_q$  is the Clifford transformation on qubit  $q$ . We refer to  $\mathcal{C}_\ell$  as the CSS or original code and  $\mathcal{C}'_\ell$  as the deformed code.

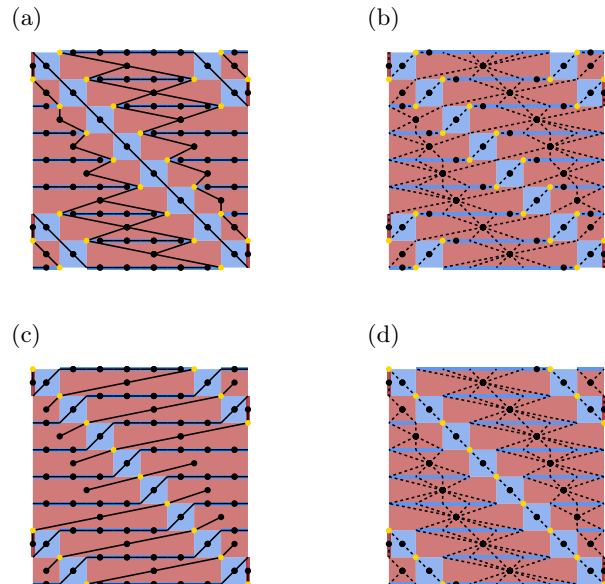


Figure 3: XZZX $\square$  and ZXXZ $\square$  deformations

Graphs of low/high-weight edges of  $\ell = 6$  elongated compass code with XZZX $\square$  deformation (a/b) and ZXXZ $\square$  deformation (c/d). Black dots represent stabilizers and yellow dots indicate the qubits that undergo a Hadamard transformation according to the deformation on the code. a) The low-weight edges divide the lattice into disjoint regions. This restricts the spread of syndromes due to high-rate errors. b) The high-weight edges create a highly connected graph, allowing defects to spread across the lattice. c) In the case of the ZXXZ $\square$  deformation, the graph of low-weight edges is composed of disjoint strings which are easy to decode. d) The high-weight graph is divided into disjoint regions which restrict the spread of defects. Note that these graphs are more easy to decode in comparison to the low-weight and high-weight graphs of the XZZX $\square$ -deformed compass codes.

Recall that the location and support qubits of the stabilizers are not changed by the Clifford deformation. Thus, a syndrome  $\vec{s}$  obtained in  $\mathcal{C}'_\ell$  can also be produced on the original code  $\mathcal{C}_\ell$ . Furthermore, both syndromes will be caused by errors that are equivalent up to the Clifford transformations  $\{U_q\}_{q=0}^N$ . Syndromes are determined through the multiplication of the parity check matrix  $H'$  and the noise vector  $\vec{e}'$ ,  $H'\vec{e}' = \vec{s} = H\vec{e}$ . The stabilizers only differ by a Clifford transformation such that there exists an orthogonal projection matrix  $O_U$  that

maps the parity check matrix of  $\mathcal{C}_\ell$  to that of  $\mathcal{C}'_\ell$  according to the Clifford deformation:  $H'^\top = O_U H^\top$ . Therefore,  $(H'\vec{e}')^\top = \vec{e}'^\top H'^\top = \vec{e}'^\top O_U H^\top = (H\vec{e})^\top$  which implies that  $\vec{e} = O_U \vec{e}'$ . We conclude that a syndrome found on both codes is caused by errors that are equivalent up to the Clifford transformations.

We write errors on  $\mathcal{C}'_\ell$  as binary noise vectors  $\vec{e}'_x$  and  $\vec{e}'_z$  denoting  $X$  and  $Z$  errors respectively. The deformed code experiences errors according to the probabilities  $p'_{x,q}, p'_{y,q}, p'_{z,q}$  of having a  $X$ ,  $Y$ , or  $Z$  error respectively on qubit  $q$ . The probabilities satisfy the biased noise model defined in Section II A where  $p'_{x,q} = p_x, p'_{y,q} = p_y$  and  $p'_{z,q} = p_z$  for all  $q$  since the probabilities are uniform across the lattice. Now, we know that errors on the deformed code are equivalent to errors on the original code up to the Clifford deformation. Thus, a  $X$  error on qubit  $q$  of the deformed code, is equivalent to a  $Z$  error on the original code if  $U_q = H$  and remains the same otherwise. Furthermore, the  $X$  error occurs with probability  $p_x$  on the deformed code which implies that the undeformed code would see  $Z$  errors with probability  $p_x$ . In general, the probabilities of  $X$  and  $Z$  errors switch for those qubits that experience a Hadamard transformation and remain the same otherwise (Eq. 3). As a result, the noise model on the undeformed code is:

$$p_{x,q} = \begin{cases} p_x & U_q = I \\ p_z & U_q = H \end{cases} \quad p_{z,q} = \begin{cases} p_z & U_q = I \\ p_x & U_q = H \end{cases} \quad (3)$$

As a result, we can decode the syndromes on  $\mathcal{C}'_\ell$  using the CSS decoder graphs of  $\mathcal{C}_\ell$  with weights modified according to the inhomogeneous noise model. After decoding, we apply the Clifford transformations to the recovery operators to obtain the appropriate correction to be applied on  $\mathcal{C}'_\ell$ .

We can see the effect of bias on our decoder by looking at the weights of the edges in our decoder graphs. The input to our decoder will be the  $X$  and  $Z$  decoder graphs of the CSS code. When  $\eta = 0.5$ , all probabilities of error are the same so the edges have the same weight. However, as the bias increases, the edges of the  $X$  ( $Z$ ) decoder graphs will have edges with weights determined by  $p_z$  ( $p_x$ ) corresponding to qubits that don't undergo a Clifford deformation and  $p_x$  ( $p_z$ ) for qubits that do. Using this, we can classify the edges on the  $X$  and  $Z$  decoder graphs as either having high weight (low probability of error) or low weight (high probability of error).

In Figure 2, we demonstrate how we classify the edges of the XZZX surface code. We start with the decoder graphs for the  $X$  and  $Z$  stabilizers of the surface code in Figures 2a and 2b. We distinguish between high and low weight edges by making them solid or dashed respectively. The low-weight edges from the  $X$  and  $Z$  matching graphs are combined in Figure 2c to create a graph with only low-weight edges, and high-weight edges are combined in Figure 2d. We can use the same procedure

to create high-weight and low-weight graphs for the deformed elongated compass codes. We show the resulting graphs in Figures 3, 6 and 7.

We can see the structure that the Clifford deformations add to the codes in the low-weight and high-weight graphs. In the case of the XZZX surface code, the low-weight edges form parallel lines. The high-weight edges also form parallel lines, but these are in a direction perpendicular to the low-weight edges (Figure 2). These figures illustrate why the XZZX surface code can be decoded as a set of disjoint repetition codes at infinite bias.

The low-weight graphs of the XZZX-deformed compass codes are divided into sections by edges forming diagonal lines similar to those in the graphs of the XZZX surface code (Figure 3a). A consequence of this is that the spread of syndromes due to high-rate errors is restricted to a particular section. These sections are not all one-dimensional as in the case of the XZZX surface code, but they will help the decoder correct the high-rate  $Z$  errors in comparison to the CSS compass codes. The XZZX deformation preserves many weight-2  $X$  stabilizers which gather more information on the high-rate  $Z$  errors. We can see that this appears in Figure 3a as repetition codes enclosed by diamonds. Thus, the vertices of the low-weight graph have degree of at most 4. The trade-off here is that the degree of the vertices in the high-weight graphs can be large (Figure 3b). In general, the high-weight decoder graphs are non-local so the defects due to high-weight errors can spread across the entire lattice. As a result, the decoder will have a harder time decoding the low-rate errors ( $X$  errors).

The low-weight and high-weight decoder graphs corresponding to the ZXXZ-deformed compass codes are shown in Figures 3c-3d. We observe that the low-weight graph is composed of disjoint strings which is desirable for the decoder. Additionally, it is useful to note the connectivity of the high-weight graphs is similar to that of the low-weight-graphs of the XZZX deformations. That is, the high-weight graphs are partitioned. This makes the ZXXZ-deformed compass codes more competitive at modest biases.

### III. RESULTS AND DISCUSSION

We evaluate the codes by calculating their threshold at different bias values ( $\eta$ ) for elongation parameters ( $\ell$ ) from 2 to 6. The thresholds we report are obtained through finite-size scaling fits near the threshold. Namely, near the threshold  $p_{th}$  we assume that the logical error rate is a quadratic function of  $(p - p_{th})L^{1/\nu}$  where  $p_{th}$  is the threshold,  $L$  is the distance, and  $\nu$  is a critical exponent [53].

We consider biases  $\eta \in \{0.5, \eta_\ell^*, 10, 25, 50, 100\}$ . Here,  $\eta_\ell^*$  are the optimal biases for the CSS elongated compass code with elongation parameter  $\ell$  found in [26] and listed in Section II B. We include  $\eta_\ell^*$  to compare the de-

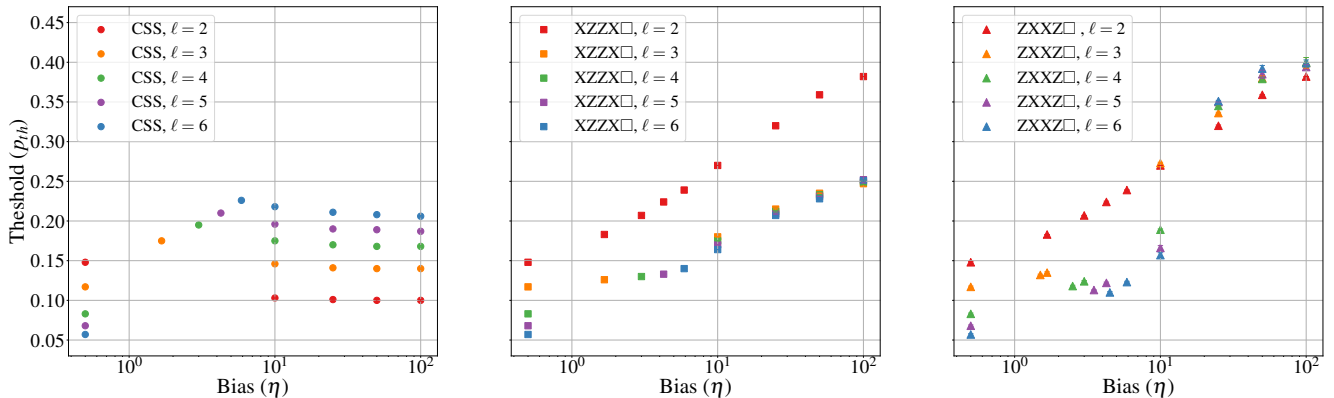


Figure 4: Thresholds for compass codes without deformation (CSS), XZZX $\square$ -deformed and ZXXZ $\square$ -deformed elongated compass codes going from left to right respectively. Thresholds are reported for codes with elongation parameters  $\ell = 2, 3, 4, 5, 6$  under noise models with bias  $\eta$ . The values of bias are on the horizontal axis starting with  $\eta = 0.5$ , corresponding to no bias. Note that the CSS, XZZX $\square$ -deformed and ZXXZ $\square$ -deformed codes have the same thresholds at  $\eta = 0.5$  since the codes are equivalent in our decoding scheme. We also note that the two deformations on the compass code with  $\ell = 2$  correspond to the XZZX surface code and thus have the same thresholds. The CSS compass codes have a maximum threshold at  $\eta_\ell^*$  and flatten out as the bias approaches infinity. The thresholds of the XZZX $\square$ -deformed compass codes increase with bias and the advantages of a higher  $\ell$  reduce as the bias increases. The thresholds of the ZXXZ $\square$ -deformed compass codes grow faster with bias compared to the XZZX $\square$ -deformed codes. These thresholds exceeded the XZZX surface code thresholds for biases  $10 < \eta \leq 100$ . Values for the thresholds shown here are recorded in Table I.

formed compass codes to the optimal performance of the CSS compass codes. The higher biases are representative of the biases found in various quantum computing architectures [8–11, 18–21].

All threshold values are listed in Table I and shown in Figure 4. When  $\eta = 0.5$ , the CSS, XZZX $\square$ -deformed and ZXXZ $\square$ -deformed compass codes are equivalent in our decoding scheme so they have the same threshold. We note that we considered finite size effects which have been shown to be significant on Clifford deformed codes [54]. To ensure convergence of the threshold, we performed simulations of the codes at high distances. For more details on this, see Appendix 3.

The CSS compass codes reach a maximum threshold at the optimal biases  $\eta_\ell^*$  and these maximum thresholds increase with  $\ell$  as expected. For each  $\ell$ , the thresholds of the CSS compass codes asymptote to the  $Z$  threshold of the codes at depolarizing noise as the bias increases. Larger elongation parameters are preferable on CSS compass codes for noise models with biased  $Z$  errors.

The thresholds of the XZZX $\square$ -deformed compass increase with bias for all elongation parameters considered. We can attribute this improvement to the fact that there are regions of the lattice to which the syndromes are confined. However, higher elongation parameters don't improve the thresholds further as the bias increases for codes with  $\ell > 2$ . This is not surprising since the general structure of the low-weight decoder graphs for the XZZX-deformed compass codes with  $\ell > 2$  looks like

that shown in Figure 3a. All of the graphs composed of lower weight edges are partitioned by the diagonals formed by the XZZX stabilizers. Between these diagonals, there are chains of diamonds each enclosing a string of length  $\ell - 2$ . The graphs composed of higher weight edges have similar structure, but they have vertices of higher degree vertices as the elongation parameter grows which can slow down the rate at which the thresholds increase with bias.

The thresholds of the ZXXZ $\square$ -deformed compass codes increase with bias and surpass the XZZX surface code thresholds for moderate biases (Figure 4). This improvement begins between  $\eta = 10$  and  $\eta = 25$  and is still observed when  $\eta = 100$ . Increasing the elongation parameter on these codes does lead to further improvement, but it becomes less relevant as the bias gets higher. We can understand the rapid increase in the thresholds by noting that both the low-weight and high-weight graphs of the ZXXZ $\square$ -deformed codes (Figure 3c-3d) restrict the spread of defects, which is not the case for the high-weight graphs of the XZZX $\square$ -deformed codes (Figure 3b). The XZZX surface code wins at lower biases because the high-weight graphs of the ZXXZ $\square$ -deformed codes have a higher degree than that of the XZZX surface code. As the bias increases, the high-weight graph becomes less relevant in the decoding process.

We also compare the logical error rates of the codes at physical error rates  $p = 0.05$  and  $p = 0.10$ . The ZXXZ $\square$ -deformed compass codes have the lowest logical error rates of the codes we consider at biases  $10 \leq \eta \leq 100$ .

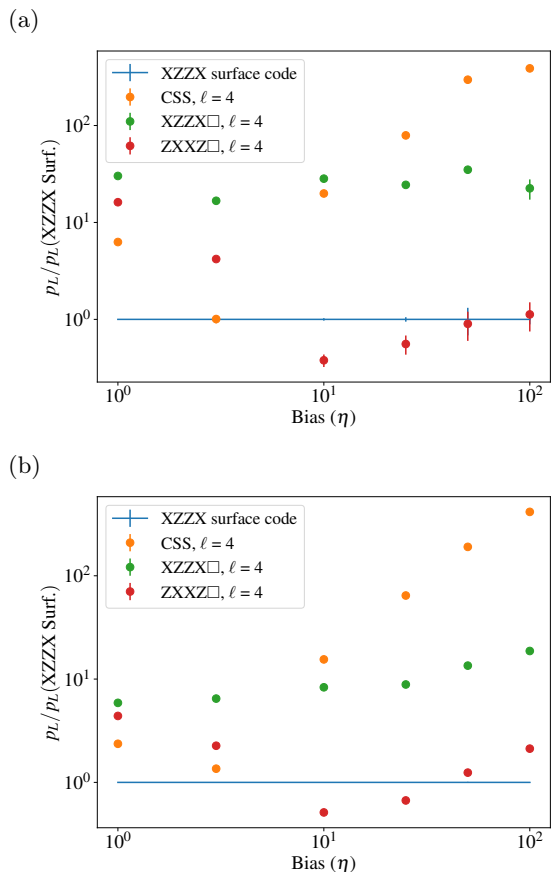


Figure 5: Logical error rates of distance 19 CSS, XZZX $\square$ -deformed and ZXXZ $\square$ -deformed compass codes with  $\ell = 4$  at **a)**  $p = 0.05$  and at **b)**  $p = 0.10$  normalized by the corresponding logical error rate of the XZZX surface code. We see that the ZXXZ $\square$  and XZZX $\square$ -deformed codes suppress the logical error rate more than the CSS code for  $\eta > 10$ . The ZXXZ $\square$ -deformed code has the lowest logical error rates at moderate biases and achieves lower logical error rates than the XZZX surface code at some biases.

We compare the logical error rates to those of the XZZX surface code by plotting their ratios in Figure 5 for codes with  $\ell = 4$ . We see similar behavior for higher elongation parameters. The CSS compass codes perform best at low biases, but their logical error rates grow much faster in comparison to those of the other codes the bias increases. The logical error rates of the ZXXZ $\square$  deformed codes are comparable to those of the XZZX surface code for biases greater than 10.

Data and source code related to this work can be accessed from [55].

#### IV. CONCLUSION

Clifford deformations [27, 29, 30] and compass codes [26, 31, 34] have both been studied in the context of biased noise models. Elongated compass codes are a particular class of compass codes that are created by fixing gauges according to a set of rules dictated by the elongation parameter  $\ell$ . Their performance improved in comparison to the surface code under noise models biased towards dephasing, but the asymmetry in the stabilizers is such that their performance is optimized at a particular bias. As a result, we considered the ZXXZ $\square$  and XZZX $\square$  deformations on elongated compass codes which preserve the weight-2  $X$  stabilizers while simplifying the structure of the decoding graphs. The resulting codes have thresholds that increase with bias.

The high weight of the stabilizers of the Clifford deformed elongated compass codes with high  $\ell$  may make their implementation unattractive in comparison to the XZZX surface code. However, we find that the thresholds of the ZXXZ $\square$ -deformed compass codes surpass those of the XZZX surface code for experimentally relevant biases. Furthermore, these codes also demonstrate an improvement in logical error rate over the XZZX surface code (Figure 5).

The success of Clifford deformed stabilizer codes under biased noise models is now starting to be explored beyond the scope of circuit-based quantum computing. Bias-preserving XZZX cluster states have shown that Clifford deformations can also be translated to QEC in measurement-based (MBQC) and fusion-based quantum computing [56, 57]. In a similar fashion, we can apply appropriate Clifford deformations to non-foliated cluster states [58, 59] by looking at their effect on the state's decoder graphs.

#### V. ACKNOWLEDGEMENTS

The authors thank S. Huang, B. Pato, and Y. Lin for valuable discussions. This work was supported by the NSF QLCI for Robust Quantum Simulation (OMA-2120757), and the ARO/LPS QCISS program (W911NF-21-1-0005), and the Office of the Director of National Intelligence (ODNI), Intelligence Advanced Research Projects Activity (IARPA), under the Entangled Logical Qubits program through Cooperative Agreement Number W911NF-23-2-0216.

[1] A. R. Calderbank and P. W. Shor, Phys. Rev. A **54**, 1098 (1996).

[2] E. Knill, R. Laflamme, and W. H. Zurek, Science **279**, 342 (1998).

- [3] D. Aharonov and M. Ben-Or, in *Proceedings of the twenty-ninth annual ACM symposium on Theory of computing* (1997) pp. 176–188.
- [4] H. Bombin, G. Duclos-Cianci, and D. Poulin, *New J. of Physics*. **14**, 073048 (2012).
- [5] Y. Tomita and K. M. Svore, *Phys. Rev. A* **90**, 062320 (2014).
- [6] S. Bravyi, M. Suchara, and A. Vargo, *Phys. Rev. A* **90**, 032326 (2014).
- [7] K. Sahay and B. J. Brown, *PRX Quantum* **3**, 010310 (2022).
- [8] A. Grimm, N. E. Frattini, S. Puri, S. O. Mundhada, S. Touzard, M. Mirrahimi, S. M. Girvin, S. Shankar, and M. H. Devoret, *Nature (London)* **584**, 205 (2020).
- [9] R. Lescanne, M. Villiers, T. Peronnin, A. Sarlette, M. Delbecq, B. Huard, T. Kontos, M. Mirrahimi, and Z. Leghtas, *Nature (London)* **16**, 509 (2020).
- [10] C. Berdou, A. Murani, U. Reglade, W. C. Smith, M. Villiers, J. Palomo, M. Rosticher, A. Denis, P. Morfin, M. Delbecq, *et al.*, *PRX Quantum* **4**, 020350 (2023).
- [11] A. Bocquet, Z. Leghtas, U. Reglade, R. Gautier, J. Cohen, A. Marquet, E. Albertinale, N. Pankratova, M. Hallén, F. Rautschke, *et al.*, *Bulletin of the American Physical Society* (2024).
- [12] K. S. Chou, T. Shemma, H. McCarrick, T.-C. Chien, J. D. Teoh, P. Winkel, A. Anderson, J. Chen, J. C. Curtis, S. J. de Graaf, *et al.*, *Nature Physics* , 1 (2024).
- [13] A. Kubica, A. Haim, Y. Vaknin, H. Levine, F. Brandão, and A. Retzker, *Physical Review X* **13**, 041022 (2023).
- [14] J. D. Teoh, P. Winkel, H. K. Babla, B. J. Chapman, J. Claes, S. J. de Graaf, J. W. Garmon, W. D. Kalfus, Y. Lu, A. Maiti, *et al.*, arXiv preprint arXiv:2212.12077 (2022).
- [15] I. Cong, H. Levine, A. Keesling, D. Bluvstein, S.-T. Wang, and M. D. Lukin, *Phys. Rev. X* **12**, 021049 (2022).
- [16] Y. Wu, S. Kolkowitz, S. Puri, and J. D. Thompson, *Nature (London)* **13**, 4657 (2022).
- [17] M. Kang, W. C. Campbell, and K. R. Brown, *PRX Quantum* **4**, 020358 (2023).
- [18] D. Nigg, M. Mueller, E. A. Martinez, P. Schindler, M. Hennrich, T. Monz, M. A. Martin-Delgado, and R. Blatt, *Science* **345**, 302 (2014).
- [19] C. Ballance, T. Hartly, N. Linke, M. Sepiol, and D. Lucas, *Phys. Rev. Lett.* **117**, 060504 (2016).
- [20] J. Taylor, H.-A. Engel, W. Dür, A. Yacoby, C. Marcus, P. Zoller, and M. Lukin, *Nature (London)* **1**, 177 (2005).
- [21] P. Aliferis, F. Brito, D. P. DiVincenzo, J. Preskill, M. Steffen, and B. M. Terhal, *New J. of Physics*. **11**, 013061 (2009).
- [22] S. Rosenblum, P. Reinhold, M. Mirrahimi, L. Jiang, L. Frunzio, and R. J. Schoelkopf, *Science* **361**, 266 (2018).
- [23] D. K. Tuckett, S. D. Bartlett, and S. T. Flammia, *Phys. Rev. Lett.* **120**, 050505 (2018).
- [24] D. K. Tuckett, A. S. Darmawan, C. T. Chubb, S. Bravyi, S. D. Bartlett, and S. T. Flammia, *Phys. Rev. X* **9**, 041031 (2019).
- [25] A. M. Stephens, W. J. Munro, and K. Nemoto, *Phys. Rev. A* **88**, 060301 (2013).
- [26] M. Li, D. Miller, M. Newman, Y. Wu, and K. R. Brown, *Phys. Rev. X* **9**, 021041 (2019).
- [27] J. P. Bonilla Ataides, D. K. Tuckett, S. D. Bartlett, S. T. Flammia, and B. J. Brown, *Nature Commun.* **12**, 2172 (2021).
- [28] K. Sahay, J. Jin, J. Claes, J. D. Thompson, and S. Puri, *Phys. Rev. X* **13**, 041013 (2023).
- [29] A. Dua, A. Kubica, L. Jiang, S. T. Flammia, and M. J. Gullans, *PRX Quantum* **5**, 010347 (2024).
- [30] K. Tiurev, P.-J. H. Derks, J. Roffe, J. Eisert, and J.-M. Reiner, *Quantum* **7**, 1123 (2023).
- [31] S. Huang and K. R. Brown, *Phys. Rev. A* **101**, 042312 (2020).
- [32] A. Paetznick and B. W. Reichardt, *Phys. Rev. Lett.* **111**, 090505 (2013).
- [33] H. Bombín, *New J. of Physics*. **17**, 083002 (2015).
- [34] B. Pato, J. W. Staples Jr, and K. R. Brown, arXiv preprint arXiv:2405.09287 (2024).
- [35] A. Y. Kitaev, *Annals of physics* **303**, 2 (2003).
- [36] E. Dennis, A. Kitaev, A. Landahl, and J. Preskill, *Journal of Mathematical Physics* **43**, 4452 (2002).
- [37] A. G. Fowler, A. C. Whiteside, and L. C. Hollenberg, *Phys. Rev. Lett.* **108**, 180501 (2012).
- [38] J. F. San Miguel, D. J. Williamson, and B. J. Brown, *Quantum* **7**, 940 (2023).
- [39] K. Tiurev, A. Pesah, P.-J. H. Derks, J. Roffe, J. Eisert, M. S. Kesselring, and J.-M. Reiner, arXiv preprint arXiv:2307.00054 (2023).
- [40] D. M. Debroy, L. Egan, C. Noel, A. Risinger, D. Zhu, D. Biswas, M. Cetina, C. Monroe, and K. R. Brown, *Physical Review Letters* **127**, 240501 (2021).
- [41] *Nature* **614**, 676 (2023).
- [42] D. W. Kribs, R. Laflamme, D. Poulin, and M. Lesosky, arXiv preprint quant-ph/0504189 (2005).
- [43] D. Poulin, *Phys. Rev. Lett.* **95**, 230504 (2005).
- [44] D. Gottesman, *Stabilizer codes and quantum error correction* (California Institute of Technology, 1997).
- [45] K. Kugel and D. Khomskii, *Zh. Eksp. Teor. Fiz* **64**, 1429 (1973).
- [46] J. Dorier, F. Becca, and F. Mila, *Phys. Rev. B* **72**, 024448 (2005).
- [47] B. Douçot, M. Feigel’Man, L. Ioffe, and A. Ioselevich, *Phys. Rev. B* **71**, 024505 (2005).
- [48] P. W. Shor, *Phys. Rev. A* **52**, R2493 (1995).
- [49] D. Bacon, *Phys. Rev. A* **73**, 012340 (2006).
- [50] A. Steane, *Proceedings of the Royal Society of London. Series A: Mathematical, Physical and Engineering Sciences* **452**, 2551 (1996).
- [51] J. Edmonds, *Canadian Journal of mathematics* **17**, 449 (1965).
- [52] O. Higgott, *ACM Transactions on Quantum Computing* **3**, 1 (2022).
- [53] C. Wang, J. Harrington, and J. Preskill, *Annals of Physics* **303**, 31 (2003).
- [54] Y. Xiao, B. Srivastava, and M. Granath, arXiv preprint arXiv:2401.04008 (2024).
- [55] J. A. Campos and K. R. Brown, Data and code from: Clifford-deformed compass codes (2024).
- [56] J. Claes, J. E. Bourassa, and S. Puri, *npj Quantum Information* **9**, 9 (2023).
- [57] K. Sahay, J. Claes, and S. Puri, *Physical Review Letters* **131**, 120604 (2023).
- [58] N. Nickerson and H. Bombín, arXiv preprint arXiv:1810.09621 (2018).

[59] M. Newman, L. A. de Castro, and K. R. Brown, *Quantum* **4**, 295 (2020).

## APPENDIX

### 1. Table of Thresholds

		Thresholds (CSS   XZZX□   ZXXZ□)														
$\eta$	$\ell$	2			3			4			5			6		
0.5		14.8			11.7			8.3			6.8			5.7		
$\eta_\ell^*$		-			17.5	12.6	13.5	19.5	13.0	12.4	21.0	13.3	12.2	22.6	14.0	12.3
10		10.3	27.0	-	14.6	18.0	27.3	17.5	17.5	18.9	19.6	17.0	16.6	21.8	16.4	15.7
25		10.1	32.0	-	14.1	21.5	33.6	17.0	21.2	34.5	19.0	20.9	35.0	21.1	20.7	35.1
50		10.0	35.9	-	14.0	23.5	38.0	16.8	23.3	37.9	18.9	23.1	38.5	20.8	22.8	39.2
100		10.0	38.2	-	14.0	24.7	39.9	16.8	24.9	40.0	18.7	25.2	39.4	20.6	25.1	39.9

Table I: Thresholds for CSS, XZZX□-deformed and ZXXZ□-deformed compass codes at all elongation parameters and biases. When  $\eta = 0.5$ , the thresholds of codes are the same since  $p_x = p_z$  and thus the deformations don't change the weights. Also, when  $\ell = 2$ , the XZZX□ and ZXXZ□ deformations are equivalent. We record the remaining thresholds in the following way: CSS | XZZX□ | ZXXZ□. Numerical uncertainty of these threshold values do not exceed 0.8%.

### 2. Additional Decoder Graphs

We include examples of graphs containing the low and high weight edges of the decoder graphs to motivate our choices for the locations of the Hadamard transformations. An demonstration of how we obtain low and high-weight graphs is shown in Figure 2.

The low(high)-weight decoder graphs (Figures 6a-6d and 7a-7d) for the CSS compass codes correspond to the  $X(Z)$  decoder graphs since all qubits experience the noise model in Equation 1. We see that both the low and high-weight decoder graphs are highly connected.

The XZZX□-deformed codes have low-weight decoder graphs that are partitioned by the diagonals created by the weight-4 stabilizers which take the form XZZX (Figures 6b and 7b). Additionally, we see that the regions between these partitions don't increase in complexity regardless of the elongation parameter. The maximum degree of the vertices on these graphs is four. The high-weight graphs are highly connected, however, increasing decoding complexity as the elongation parameter grows (Figures 6e and 7e).

Low-weight graphs of the ZXXZ□-deformed compass codes are composed of disjoint segments or repetition codes (Figures 6c and 7c). The repetition codes are not of the same length, which could lead to more significant finite size effects (Figure 11). Additionally, the high-weight graphs (Figures 6f and 7f) are partitioned in a fashion similar to the low-weight graph of the XZZX□-deformed codes. This allows the ZXXZ□-deformed codes to suppress low rate errors more efficiently than the XZZX□-deformed codes.

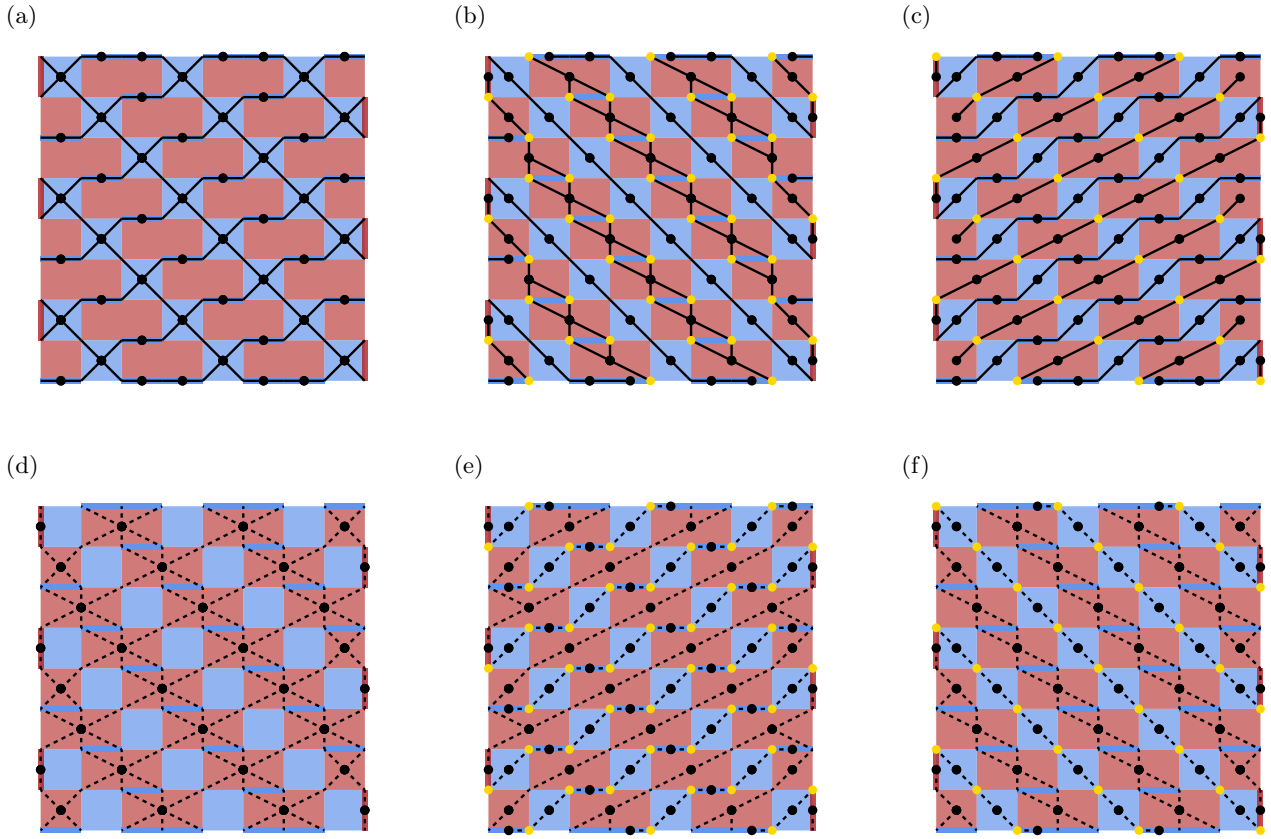


Figure 6: We list the low/high-weight graphs for the CSS (a/d), XZZX $\square$ -deformed (b/e) and ZXXZ $\square$  (c/f)-deformed compass code with  $\ell = 3$ .

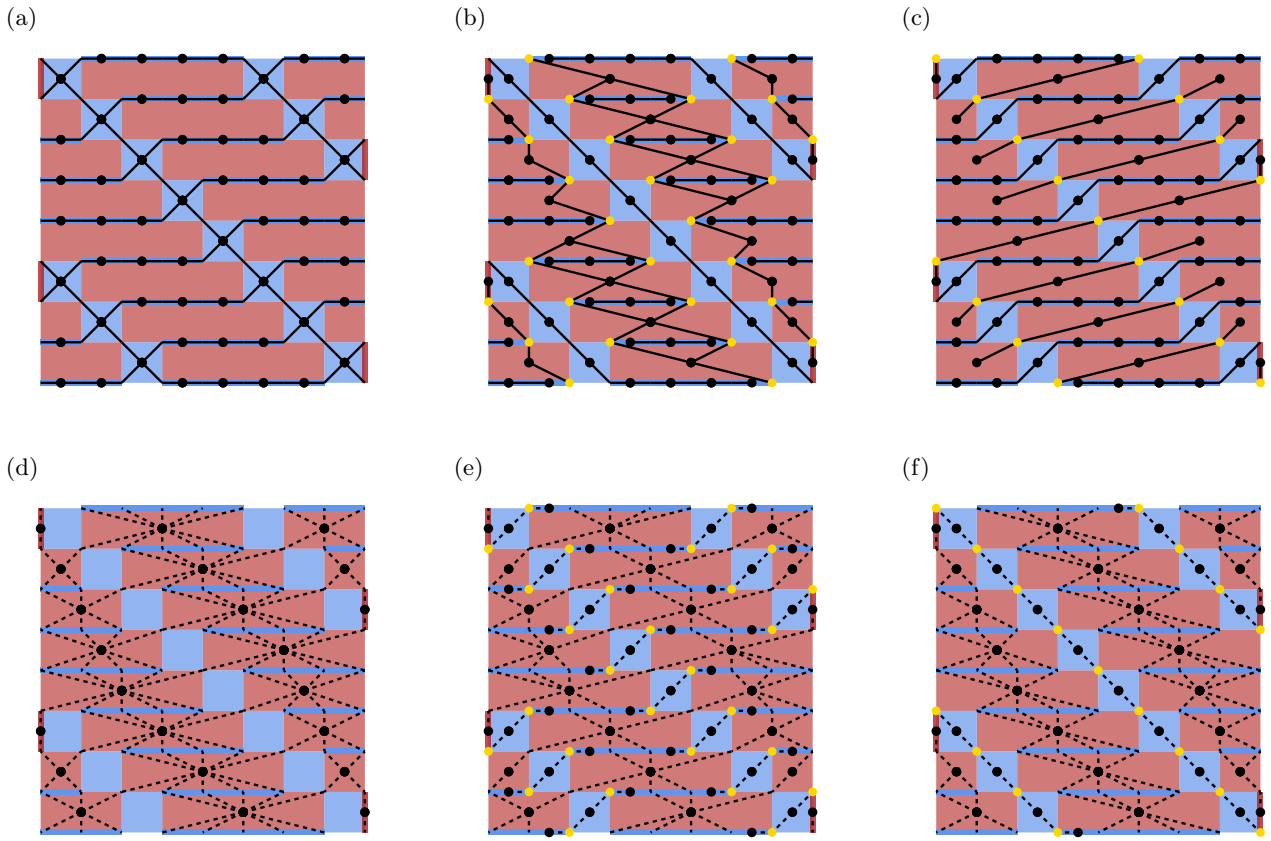


Figure 7: We list the low/high-weight graphs for the CSS (a/d), XZZX $\square$ -deformed (b/e) and ZXXZ $\square$ -deformed (c/f) compass code with  $\ell = 5$ .

### 3. Threshold Plots

The thresholds were found using finite-size scaling analysis near threshold. The numerical fit was a quadratic function of  $(p - p_{th})L^{1/\nu}$  where  $p$  is the physical error rate,  $p_{th}$  is the threshold,  $L$  is the distance and  $\nu$  is a critical parameter. Numerical fits yield threshold value and uncertainties are no greater than 0.8% for all thresholds reported in Table I. We confirmed the stability of the threshold found with respect to finite-size effects by looking at how the logical error rates fluctuated with distance.

The finite-size effects on the XZZX $\square$  and ZXXZ $\square$ - deformed compass code are significant especially as the bias increases. To minimize these effects, we calculate the thresholds using odd distances from 27 to 43 (Figure 8a). In [54], the authors calculated the magnitude of finite-size effects on the XZZX and XY surface codes and found that finite-size effects are suppressed when the distances considered are comparable to the bias. We analyze the logical error rates near threshold as a function of distance to determine how large finite-size effects are on the system sizes we considered while calculating thresholds. In the case of an XZZX $\square$ -deformed compass code with  $\ell = 3$  we determine that the threshold we found is stable even at distances smaller than those we used in our calculations (Figure 8c). Finite-size effects were more notable on ZXXZ $\square$ -deformed compass codes with a high elongation parameter under noise models with high bias (Figure 11b). For example, in Figure 11c we show that the threshold stability for the ZXXZ $\square$ -deformed compass code with  $\ell = 5$  and  $\eta = 10$  begins only after a distance of about 35. For distances below 35, we see logical error rate suppression even at a physical error rate 5% above the threshold value we found which would imply that the threshold is higher.

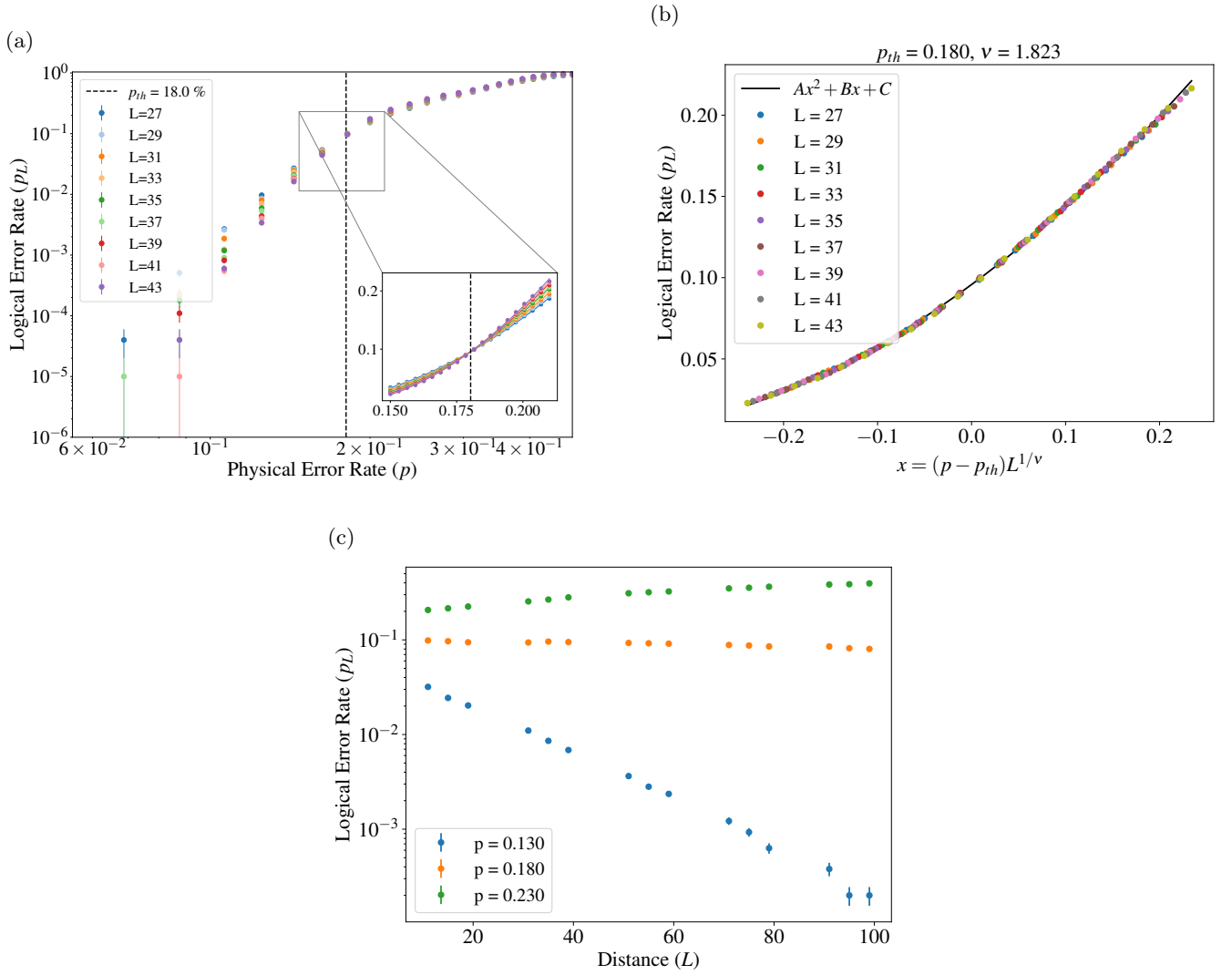


Figure 8: **a)** Threshold plot for XZZX-deformed code with elongation parameter  $\ell = 3$  and bias  $\eta = 10$ . **b)** Finite-size scaling plot corresponding to fit shown in the inset of **a**. **c)** Plot of logical error rates versus distances for physical error rates below ( $p = 0.13$ ), at ( $p = 0.18$ ), and above ( $p = 0.23$ ) threshold. We observe that the logical error rate remains constant at the threshold while it decreases (increases) for physical error rates below (above) threshold.

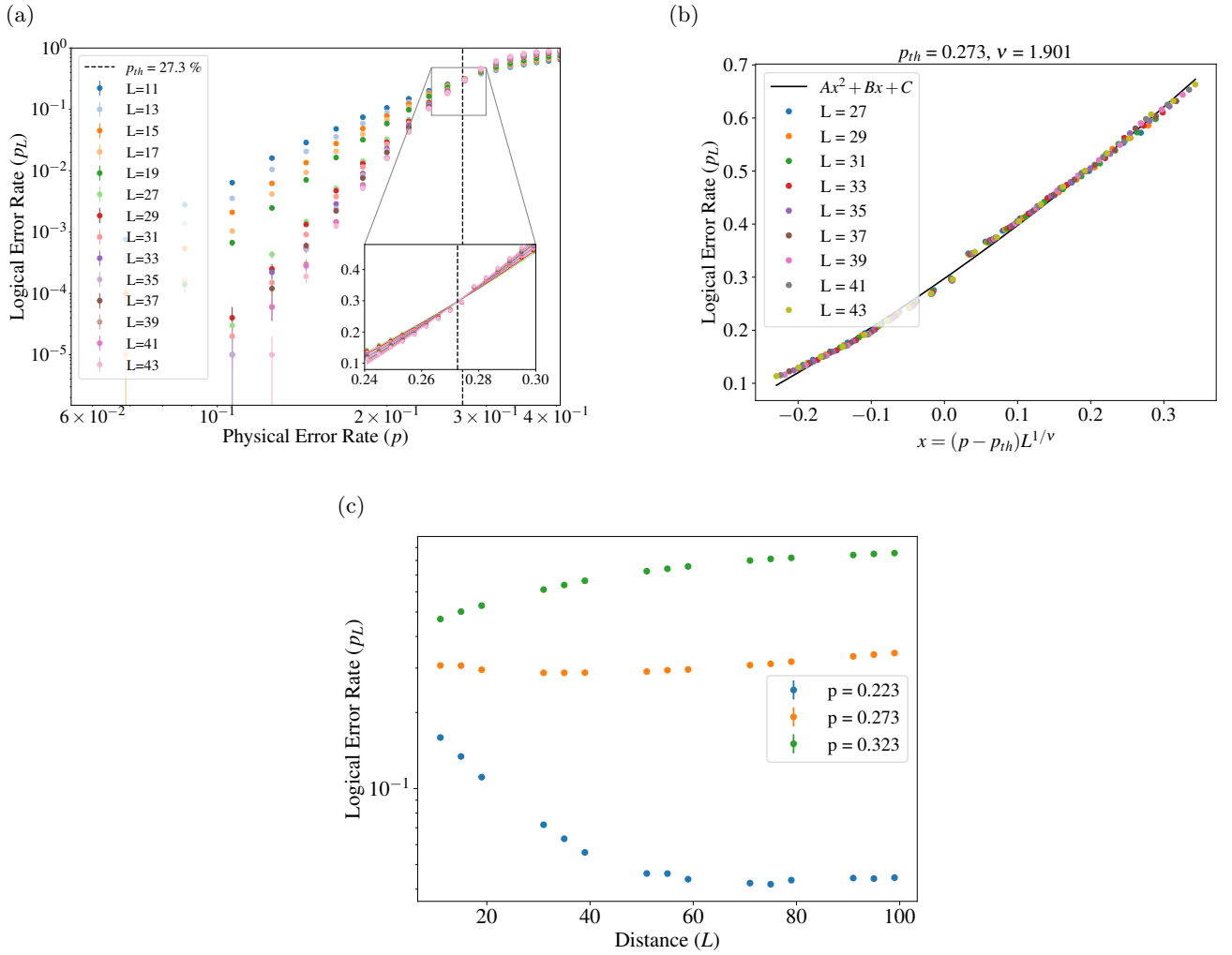


Figure 9: **a)** Threshold plot for ZXXZ-deformed code with elongation parameter  $\ell = 3$  and bias  $\eta = 10$ . **b)** Finite-size scaling plot corresponding to fit shown in the inset of **a**. The fit is applied on curves with distances 27-43. We include curves of lower distances in **a** to show that all curves intersect near the threshold value reported. **c)** Plot of logical error rates versus distances for physical error rates below threshold ( $p = 0.223$ ), at threshold ( $p = 0.273$ ), and above threshold ( $p = 0.323$ ) threshold. We observe that the logical error rate remains constant at the threshold while it decreases (increases) for physical error rates below (above) threshold.

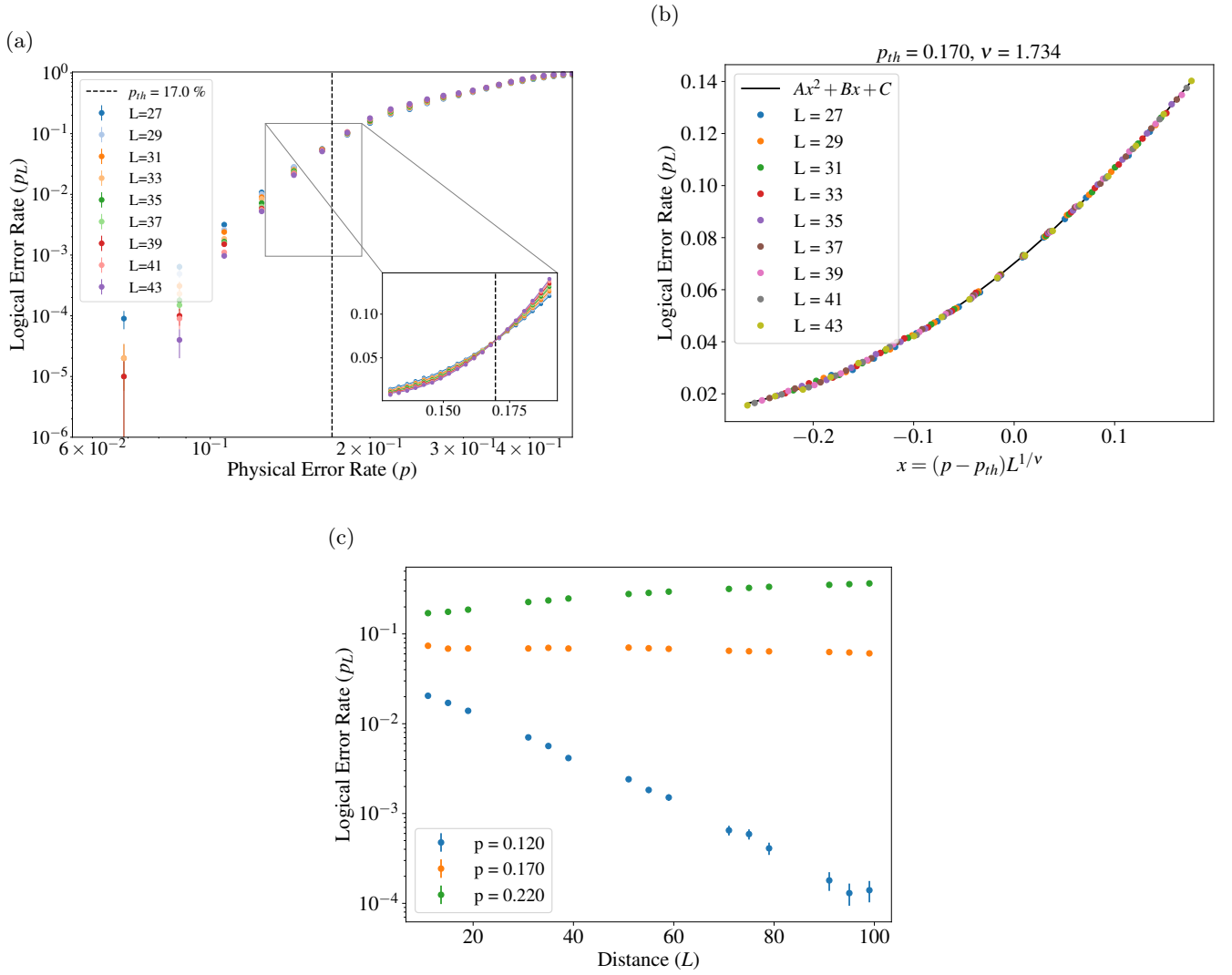


Figure 10: **a)** Threshold plot for XZZX-deformed code with elongation parameter  $\ell = 5$  and bias  $\eta = 10$ . **b)** Finite-size scaling plot corresponding to fit shown in the inset of **a**. **c)** Plot of logical error rates versus distances for physical error rates below ( $p = 0.12$ ), at ( $p = 0.17$ ), and above ( $p = 0.22$ ) threshold. We observe that the logical error rate remains constant at the threshold while it decreases (increases) for physical error rates below (above) threshold.

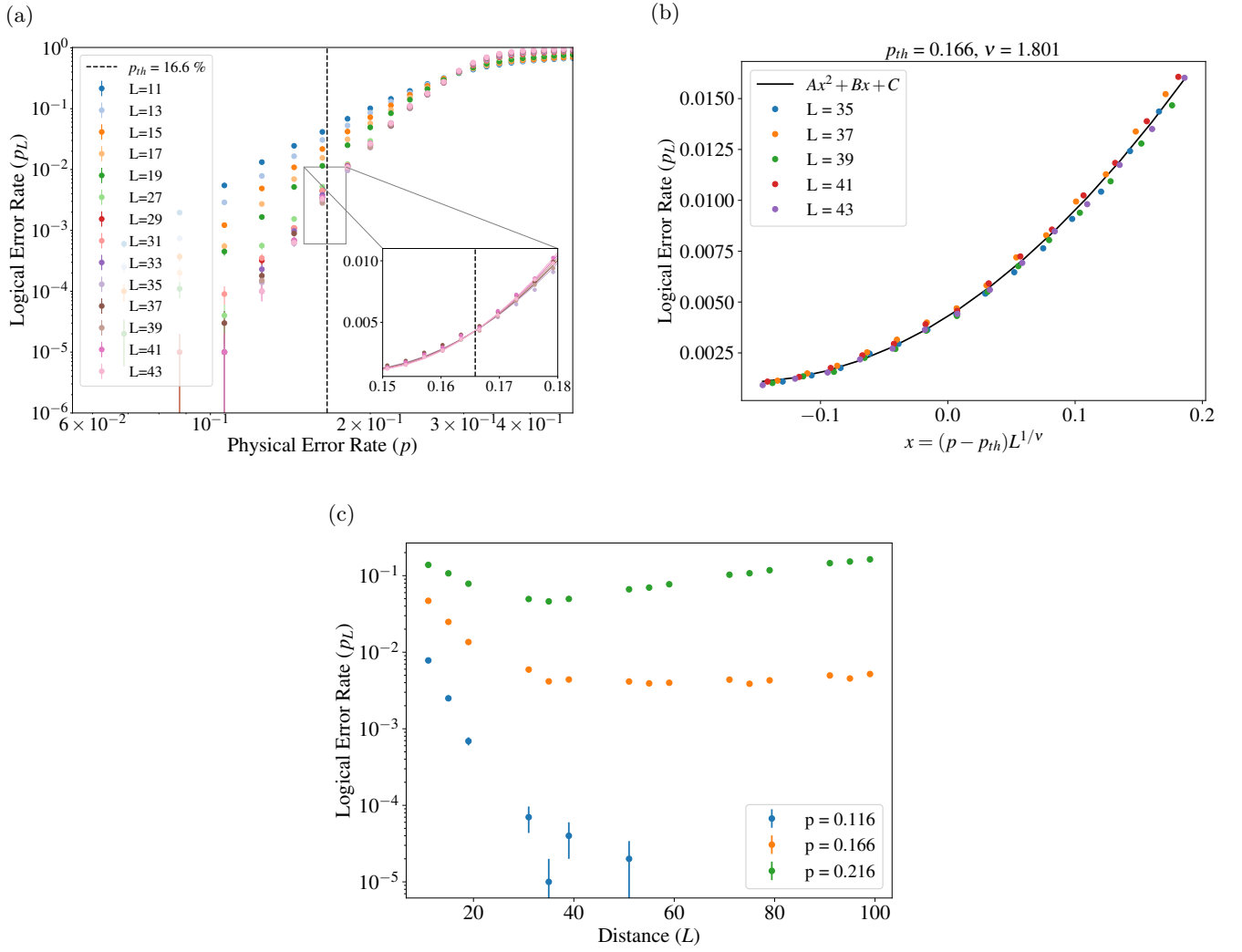


Figure 11: **a)** Threshold plot for ZXXZ-deformed code with elongation parameter  $\ell = 5$  and bias  $\eta = 10$ . **b)** Finite-size scaling plot corresponding to fit shown in the inset of **a**. **c)** Plot of logical error rates versus distances for physical error rates below ( $p = 0.116$ ), at ( $p = 0.166$ ), and above ( $p = 0.216$ ) threshold. In **a**, we see two different physical error rates at which groups of the curves cross. The set of curves that intersect at the larger physical error rate have smaller distances, indicating that they suffer from finite-size effects. From **c**, we observe how the logical error rates at the threshold value decreases for distances less than  $L = 35$  which would indicate that we threshold is higher than what we report. However, the logical error rates at the threshold value stabilize after that distance.